Hindawi Publishing Corporation
International Journal of Microwave Science and Technology
Volume 2010, Article ID 535307, 9 pages
doi:10.1155/2010/535307

Research Article

Design and Comparison of 24 GHz Patch Antennas on Glass Substrates for Compact Wireless Sensor Nodes

Florian Ohnimus,[1] Uwe Maaß,[2] Gerhard Fotheringham,[2] Brian Curran,[2] Ivan Ndip,[2] Thomas Fritzsch,[2] Jürgen Wolf,[2] Stephan Guttowski,[2] and Klaus-Dieter Lang[2]

[1] *Berlin Institute of Technology, Technische Universität Berlin, Straße des 17. Juni 135, 10623 Berlin, Germany*
[2] *Fraunhofer Institute for Reliability and Microintegration (IZM), Gustav-Meyer-Allee 25, 13355 Berlin, Germany*

Correspondence should be addressed to Florian Ohnimus, florian.ohnimus@izm.fraunhofer.de

Received 9 September 2010; Revised 24 November 2010; Accepted 9 December 2010

Academic Editor: Chien-Jen Wang

Three patch antennas suitable for integration and operation in a compact 24 GHz wireless sensor node with radar and communication functions are designed, characterized, and compared. The antennas are manufactured on a low loss glass wafer using thin film (BCB/Cu) wafer level processing (WLP) technologies. This process is well suited for 3D stacking. The antennas are fed through a microstrip line underneath a ground plane coupling into the patch resonator through a slot aperture. Linear polarization (LP), dual mode (DM) operation, and circular polarization (CP) are achieved through the layout of the slot aperture and rectangular patch dimensions. Antenna gain values of ~5.5 dBi are obtained in addition to the 10 dB impedance bandwidths of 900 MHz and 1.3 GHz as well as 500 MHz CP bandwidth with a 3 dB axial ratio for the LP, DM, and CP patch antennas, respectively.

1. Introduction

Autarkic wireless sensor networks are becoming widespread in industrial applications and have been in the focus of many research activities [1]. The development and application of tiny radio sensor nodes that are equipped with radar and communication functions are of interest for gathering spatial information in addition to sensor information [2]. The 24 GHz unlicensed ISM (industrial, scientific, and medical) frequency band, with a free space wavelength of 12.5 mm, allows the realization of radar with a spatial resolution in the cm-range. There is also more bandwidth (250 MHz) available for frequency modulated communication and radar signals compared to the popular ISM band at 2.4 GHz. Another advantage of the short wavelength is that efficient antennas can be realized for integration in the sensor node platform increasing the miniaturization potential.

The integrated antenna plays a crucial role in the overall system performance of such sensor node applications. To date, much research has focused on planar antenna designs for quasi millimeter-wave applications using PCB or LTCC technologies [3–5]. However, highly integrated sensor node platforms comprise compact 3D stacks, where the antenna is integrated in one of the stack modules [6–8]. For this purpose, antenna designs suitable for 3D stacks and thin film processing have been reported. These include patch antennas processed directly on silicon substrates [9]. Since silicon substrates are lossy, micromachining techniques [10], used to create cavities, and high resistivity silicon (HRS) substrates [11] have been employed to increase the antenna efficiency. These approaches, however, lead to high costs. Therefore, in order to overcome this limitation, glass substrates, as an alternative to silicon, are considered for planar antenna integration in this work. Glass possesses lower dielectric losses compared to silicon and is also processable using thin film technologies.

Figure 1 shows the concept of the integration platform of the compact wireless sensor node. The top module comprises the components (e.g., the active RFICs and embedded passive components) of the RF front-end including the

integrated planar antenna. The second module includes the IF and baseband components. Both modules can be interconnected using interstack bumps in a 3D build-up.

In this work, three 24 GHz patch antennas with different modes of operation which are suitable for integration in the top RF module of the wireless sensor node are designed and characterized. The focus lies on the implementation and test of these antennas at 24 GHz in combination with thin film technologies and fabrication on a glass substrate. A comparison of the antennas based on full-wave simulations and measurements is conducted.

This paper is divided into three sections. In Section 2, the patch antenna concept and feeding techniques are explained followed by the simulation results and analysis in Section 3. The results of an experimental characterization are presented in Section 4.

2. Patch Antenna Concept and Feeding Technique

There are three basic techniques for feeding a patch antenna. These include (1) direct feeding [12, 13] such as coaxial, edge, or inset, (2) aperture coupling [14–16], and (3) proximity coupling [17, 18]. For the proposed layer stack-up in Figure 1, the aperture coupling technique offers the combined advantages that the antenna can be fed from underneath the ground plane (the ground plane also acts as a shielding layer) through an impedance controlled microstrip line and that no vias are required for galvanic contact of the patch antenna. Furthermore, the aperture coupling technique inherently allows high bandwidth operation. Figure 2 shows the electrical (a) and technological (b) concepts of the aperture coupling in the context of the above 3D build-up.

The three patch antennas are all designed to operate as $\lambda/2$ resonators on the glass substrate of height h. Two orthogonal resonance modes including the TM_{100} and TM_{010} are excitable on a square or rectangular patch geometry.

The principle electric and magnetic field distributions of the TM_{100} mode, forming a standing wave on the resonator of length l, are indicated in Figure 2(a). The dielectric properties of the glass substrate, described by the relative dielectric constant ε_{rr} and loss tangent $\tan(\delta)$, are crucial for the resonance frequency and efficiency of the antenna, respectively. The impedance controlled 50 Ω microstrip line is extended underneath the slot in the ground plane by length l_f and terminated in an open circuit. Note that the microstrip line is routed underneath the ground plane on the BCB dielectric layer. At approximately one quarter effective wavelength from the open circuit, a current maximum occurs and, hence, the H-field coupling into the patch resonator through the slot can be optimized.

Figure 2(b) shows the technological build-up. The antenna substrate comprises a glass wafer. The glass wafer is structured from both sides using thin film processing with BCB and copper (Cu). The employed glass has $\varepsilon_r = 4.6$ and a dielectric loss tangent $\tan(\delta) < 0.01$ at 24 GHz. The BCB layer between microstrip line and ground plane has a total height of 16 μm and $\varepsilon_r = 2.7$. Therefore, the microstrip feeding line requires a width of 40 μm in order to achieve a characteristic transmission line impedance of 50 Ω.

Figure 3 shows the variations of the patch antenna configuration with three modes of operation comprising: (a) linear polarization (LP), (b) dual mode (DM) operation, and (c) circular polarization (CP).

The LP patch antenna produces linear polarization. The DM patch antenna has the advantage of additional impedance bandwidth because two in-phase resonance modes are excited on the patch resonator through the cross slot. Since the modes are ideally orthogonal, they can also be used to achieve dual polarization with two separate feeds, as has been demonstrated in [19]. However, here they are excited through one feeding line to exploit the increased impedance bandwidth advantage with defined linear polarization (diagonal). These two modes can also be used to produce CP if the resonance frequencies of the two modes are separated slightly to achieve quadrature mode excitation. This has been studied theoretically in [20].

The different modes of operation are determined by the configuration of the slot aperture in the ground plane (single or cross) and by the patch dimensions (l, w). In all cases, the slot dimensions (l_s, w_s) as well as l_f are also used to fine tune the antenna input matching. In order to obtain LP, the TM_{100} mode is excited on the patch resonator through a single slot. DM is obtained by exciting both TM_{100} and TM_{010} modes in phase on a square patch resonator $(l = w)$. For CP operation, two quadrature TM modes are excited on a rectangular patch $(l \neq w)$.

3. Simulation Results and Analysis

The antennas were simulated using Ansys (formerly Ansoft) HFSS v12, a 3D full-wave simulation suite, based on the finite element method (FEM) in the frequency domain. Parameterized 3D models of the antenna structures were built comprising the geometrical and material data. The antennas are fed through a wave port backed with a perfect electrical conductor (PEC). Furthermore, perfectly matched layer (PML) boundary conditions are used to truncate the computational domain. Care was taken to ensure a high accuracy of the computed field and S-parameter solutions. The PMLs were placed at a distance of at least $\lambda/4$ at 24 GHz (3.125 mm) away from the physical antenna structure to ensure that the reactive near-fields of the excited antenna have decayed far enough to not interact with the PMLs, potentially altering the antenna characteristics. The adaptive mesh refinement in the simulation process was also used in order to ensure stability of the computed field solution. At least eight consecutive passes with a mesh refinement of 30% were computed and it was ensured that two consecutive passes produce a maximum ΔS of 0.01.

The antennas were tuned for 24 GHz operation. Using approximate analytical formulas, for example, in [21], the dimensions for obtaining resonance were roughly calculated. The full-wave simulations were then conducted for resonance frequency fine tuning and impedance matching. The optimized patch dimensions for the LP and DM patch antenna are $l = w = 2.5$ mm. The slot aperture dimensions

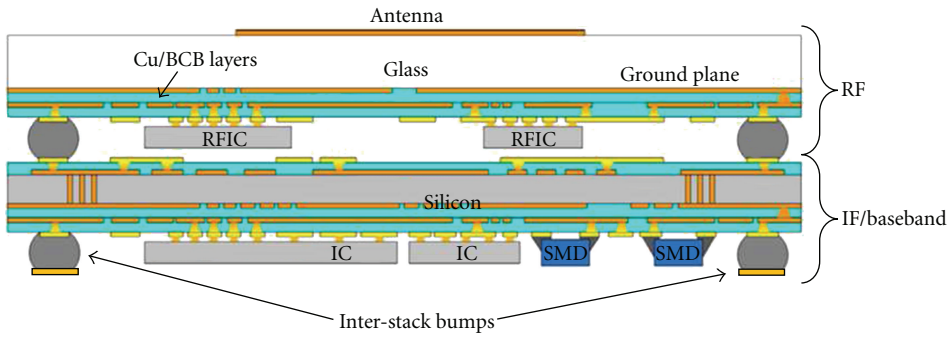

FIGURE 1: Illustrative overview of the 24 GHz 3D sensor node integration platform comprising the top RF module (on a glass substrate) with integrated antenna and the lower IF/baseband module (on a silicon substrate).

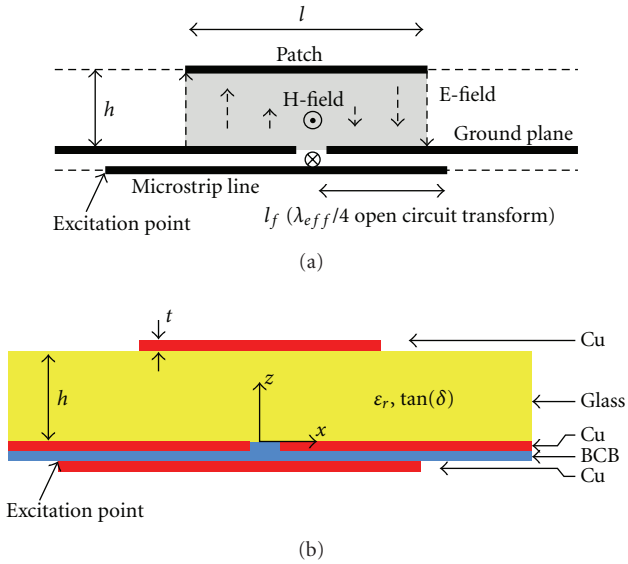

FIGURE 2: Illustration of (a) the electrical concept of aperture coupling used to feed the antennas and (b) the technological layer build-up including the glass substrate.

for obtaining impedance matching with an input reflection coefficient <-10 dB are $l_s = 1.5$ mm as well as $w_s = 150\,\mu$m and $w_s = 75\,\mu$m for the LP and DM patch antenna, respectively. Since two cross slots are used for the DM patch antenna, the slots are only half the width. The dimensions of the feeding structure of the CP patch antenna are the same as for the DM patch antenna. Only the patch dimensions are different with $l = 2.6$ mm and $w = 2.325$ mm. This ensures that the two resonances are separated to obtain CP operation in between where the phase difference between the modes is 90°. With this setup RHCP is obtained. LHCP can be obtained by switching the dimensions for l and w, which is the same as turning the rectangular patch or the feeding line by 90° relative to the center of the antenna.

In order to explain the modes of operation, the simulated current distributions on the patch antennas are shown in Figure 4.

The current distribution of the modes on the patch resonator are indicated by the surface current density $\underline{J}(x, y)$. In the case of LP (a), the current is primarily x directed. In the case of DM operation (b), the currents of the two modes are x and y directed resulting in a total current diagonally across the patch. Therefore, the polarization is also linear but diagonally across the patch. Finally, for CP operation, the two modes are 90° out of phase. To achieve this, the frequencies of the two modes are separated slightly ($l < w$)—this results in a circulating current on the patch resonator at a frequency between the two shifted resonance frequencies where the 90° phase difference condition is met.

Next, the simulated radiation pattern of the LP patch antenna is analyzed. It resembles the radiation characteristics of the TM_{100} mode. The simulation results of the E- and H-planes are shown in Figure 5. A gain of 5.5 dBi is observed. Furthermore, although the antenna is excited through a slot in the ground plane, the backward radiation is -12 dBi yielding a front-to-back ratio of 17.5 dB. Note that the size of the truncated ground plane and substrate are 8 mm × 8 mm, the envisaged length and width of the sensor node platform.

The radar function is based on measuring the relative distances between the individual sensor nodes. Therefore, the phase center of the TM_{100} mode is also of interest for the radar function. It is desirable to obtain a constant phase distribution in the top hemisphere. This is necessary since the orientation of the sensor nodes is generally not known to the sensor node network. Figure 6 shows the simulation results of the normalized phase on the surface of a sphere with radius 20 mm from the geometrical center of the antenna. The linear polarized electric fields E_θ and E_φ are plotted in the E-plane (xz) and H-plane (yz), respectively.

It is observed that the phase varies with a maximum of 2.5° for values of θ within $-75°$ to 75°. In lateral directions, it reaches a maximum change of $-7.5°$.

Concerning the circular polarization of the CP patch antenna, Figure 7 shows a plot of the simulated axial ratio over the frequency in z-direction. It is observed that the axial ratio is below 3 dB over a bandwidth of approximately 500 MHz.

Finally, in Table 1, a summary of the simulation results and comparison of the physical as well as the electrical parameters of the three patch antennas are summarized.

The physical and electrical parameters from the simulations are summarized on the LHS and RHS of the table,

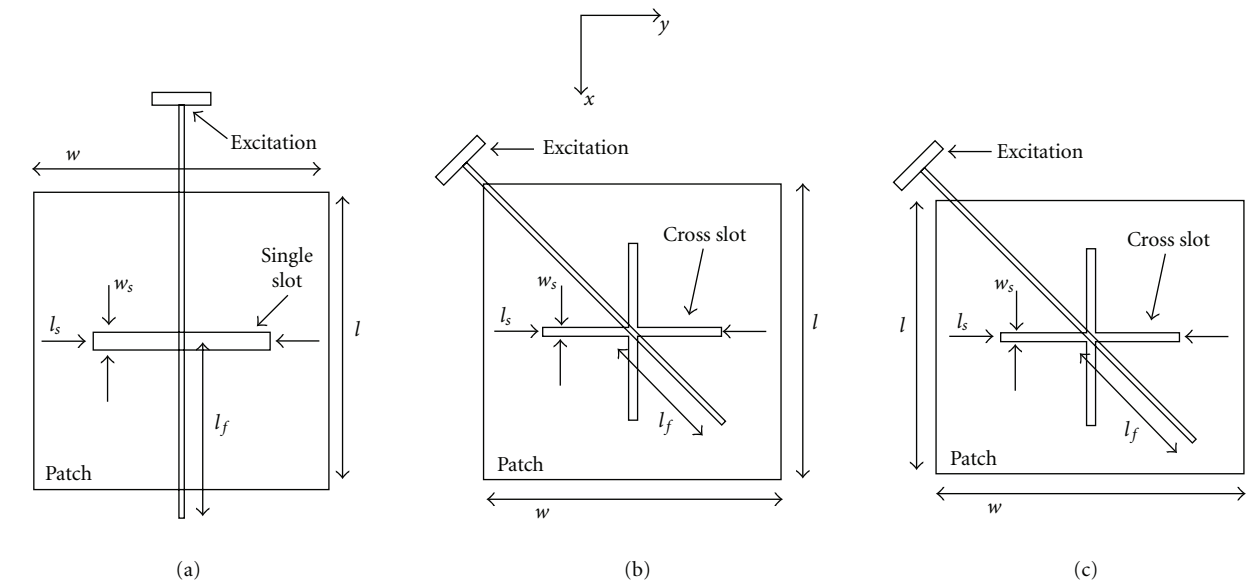

Figure 3: Illustration of the dimensions of the (a) LP, (b) DM, and (c) CP patch antennas.

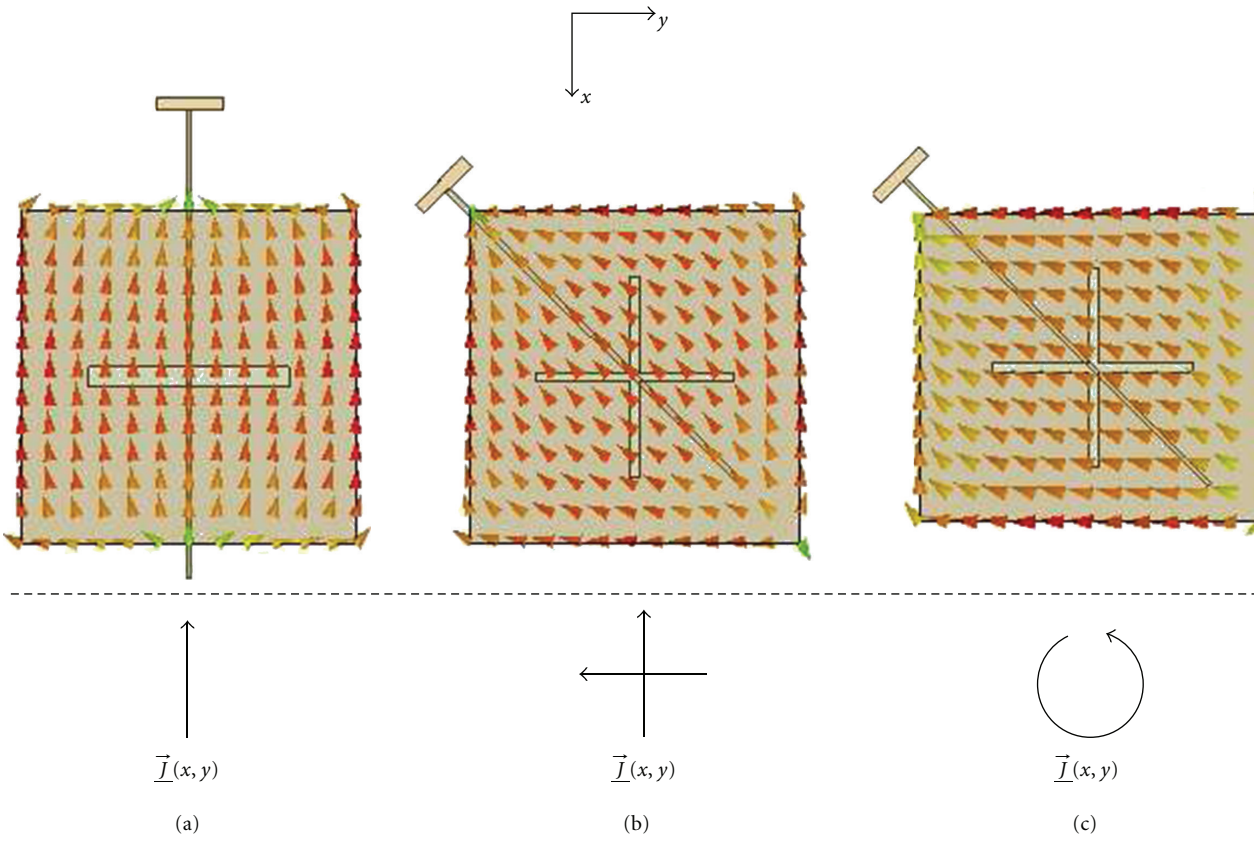

Figure 4: Illustration of the excited currents on the three patch antennas: (a) LP, (b) DM, and (c) CP operation.

respectively. The impedance bandwidth (BW) is evaluated within the frequency range where the input reflection coefficient of the antennas is below approximately −10 dB. It is observed that the DM operation results in increased bandwidth from 900 MHz to 1.3 GHz. The bandwidth for the CP patch antenna, where a 3 dB axial ratio is obtained, is obtained across a bandwidth of 500 MHz. The gains of the antennas are approximately 5.5 dBi each concerning the respective modes of radiation in the direction normal to the patch.

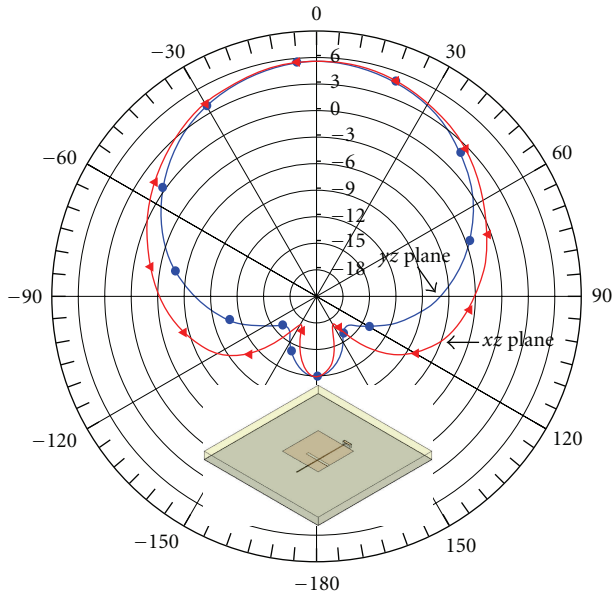

Figure 5: E-plane (xz) and H-plane (yz) radiation patterns of the LP patch antenna in decibels.

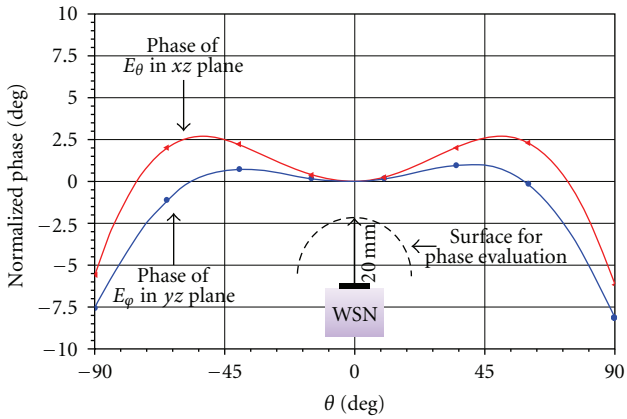

Figure 6: Simulation results of the electric field phase distribution on a spherical surface around the antenna.

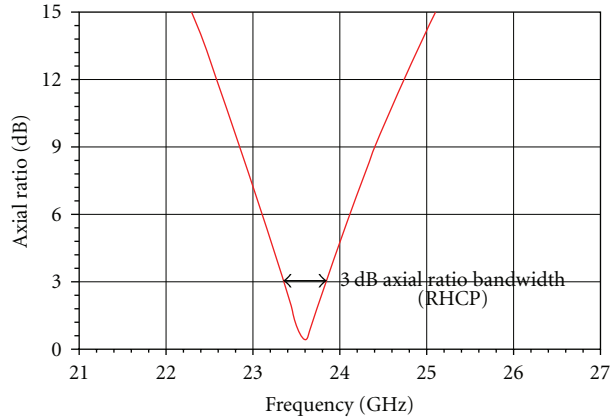

Figure 7: Plot of the simulated axial ratio of the CP patch antenna in direction normal to the patch.

Table 1: Summary and comparison of the simulated antenna parameters.

Antenna type	Physical parameters		Electrical parameters	
	Patch [mm^2]	Aperture [mm^2]	BW [GHz]	Gain [dBi]
LP	2.5×2.5	0.15×1.5 (single)	0.9	5.5
DM	2.5×2.5	0.075×1.5 (cross)	1.3	5.5
CP	2.325×2.6	0.075×1.5 (cross)	0.5 (3 dB AR)	5.5 (RHCP)

Since the simulation results need to be validated with measurements, the following section deals with the manufacturing and high frequency measurements of the antennas.

4. Experimental Characterization

The three antenna types were manufactured using IZM's thin film WLP technology. Figure 8 shows a photo of the manufactured antennas on the glass substrate. The wafer is diced in blocks of 8×8 mm^2. In Figure 9, the bottom view of two antennas are shown illustrating the feed structures with the single and cross slot apertures for the LP and DM/CP patch antennas, respectively.

A GSG (ground, signal ground) probe adapter was designed to contact the microstrip lines using a GSG probe with a pitch of 150 μm. The two outer ground pads are shorted to the ground plane using vias through the BCB layer.

Furthermore, in Figure 10 a cross section of the microstrip feeding line is shown. It is observed that the total thickness of the BCB layer is approximately 15.9 μm. The ground plane metal thickness is about 3.2 μm. Although thin, the skin depth of copper at 24 GHz is below 0.5 μm. Therefore, the ground plane is still considered a good shielding layer.

In order to characterize the input reflection coefficients and gain of the antennas, measurements were conducted. The small size of the diced antenna substrates (8 mm $\times$ 8 mm) imposes particular challenges on the handling and contacting of the antennas.

4.1. Input Reflection Coefficient Measurements. Figure 11 shows the test setup that was used to measure the input reflection coefficients of the antennas. A one port S-parameter measurement using a GSG probe (150 μm pitch) was used. The vector network analyzer (PNA 8361A) was calibrated using the SOL (short, open, load) technique to ensure that the reference planes for the S-parameter measurements are located at the probe tips.

The measurement setup comprises a piece of hardboard with a 7 mm cut slit in it to facilitate the placement of the antenna under test (AUT). The patch faces downwards "radiating through the slit in the hardboard". The feeding

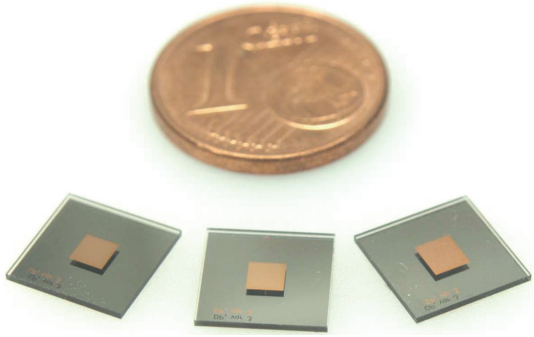

Figure 8: Photo of the three diced antenna substrates with a one euro cent coin in the background.

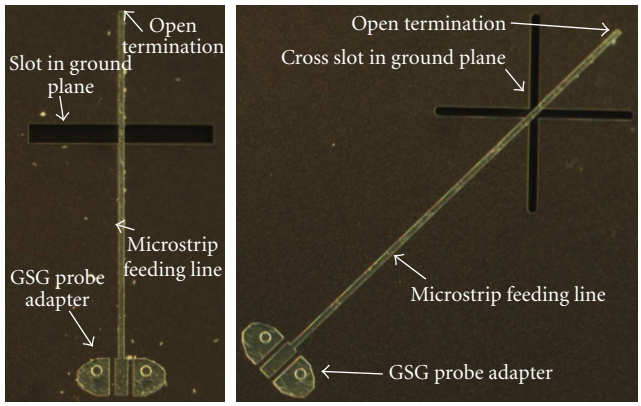

(a) (b)

Figure 9: Microscope images of the feeding structures (bottom view) of the following: (a) LP patch antenna with a single slot and (b) DM and CP patch antennas with a cross slot.

lines are contacted with the GSG probe mounted on the probe positioner. A microscope is used to place the probes.

A comparison between simulation and measurement results of the LP, DM, and CP patch antennas is depicted in Figures 12 to 14, respectively. A satisfactory correlation between measurements and simulation was obtained.

The discrepancies between measurement and simulation results are attributed to technological tolerances, measurement inaccuracies, and proximity effects of the measurement environment. The impedance bandwidths are evaluated between the −10 dB input reflection points, where 10% or less of the input power is reflected. Concerning the CP patch antenna, it is observed that the reflection coefficient between the two excited modes above and below 24 GHz is ∼ −8 dB, which is slightly higher than −10 dB. Simultaneously achieving good impedance matching condition (in comparison to the LP and DM patch antennas) as well as a low axial ratio <3 dB was found challenging. The reason for this is that the two excited resonance modes must be "sufficiently far apart" to obtain the 90° phase condition required for CP operation. Furthermore, the 500 μm thick glass (required for efficient radiation) in contrast to the thin 16 μm BCB layer used for the routing of the microstrip line further poses challenges

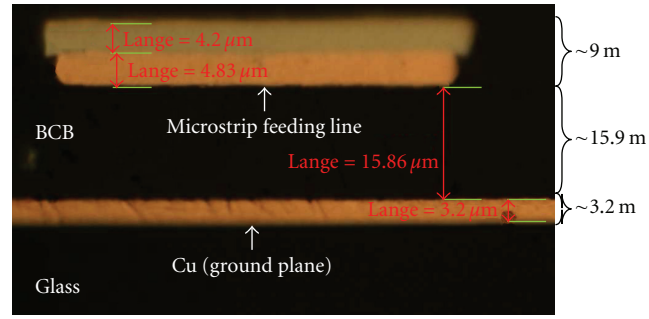

Figure 10: Measurements of the dimensions of the cross section of the microstrip feeding line comprising thin film BCB/Cu layers.

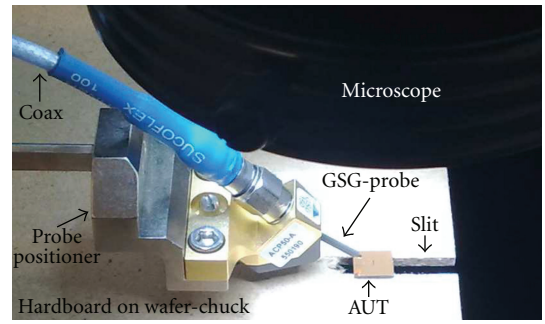

Figure 11: Measurement setup for input reflection measurements of the antennas on a wafer prober station.

on the matching. Different slot geometries for CP operation were not further investigated in this work.

The excitation of the resonance modes and operation of the patch antennas have been shown with measurements. Next, the results of the transmission measurements are presented.

4.2. Transmission Measurements. In the following, the focus is on performing transmission measurements to verify the simulated antenna gain since this is vital for showing the antenna performance. Free space transmission measurements between a standard gain horn antenna (17.5 dBi at 24 GHz) and the AUT mounted upside-down on a Styrofoam block with a separation distance of 30 cm were conducted. The Styrofoam block has favorable dielectric properties similarly to those of air. Therefore, capacitive loading of the antenna caused by the Styrofoam block is assumed negligible. Figure 15 shows the measurement setup. Stray reflection from the environment is considered minor because the horn antenna is directive and the AUT is also directed with its main radiation lobe (in the direction normal to the patch resonator, see Figure 5) towards the horn antenna.

The polarization of the horn antenna can be adjusted with Φ to illuminate the AUT with horizontal and vertical polarization, that is, $\Phi = 0°$ and 90°, respectively. Concerning the separation distance r between the horn antenna and the AUT, the far-field condition should be met in order for the free space transmission models to be used. The maximum

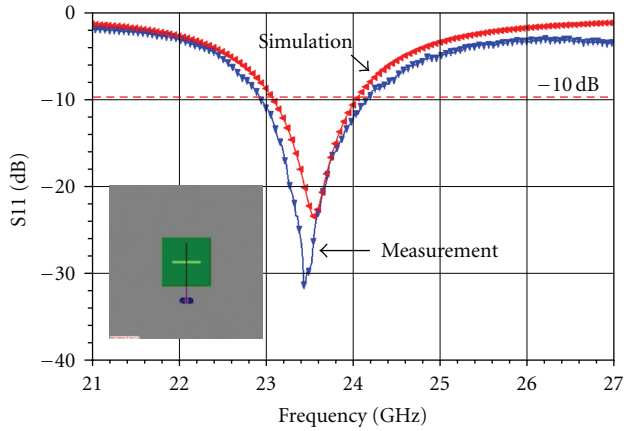

Figure 12: Measurement results of the input reflection coefficient of the linear polarized patch antenna.

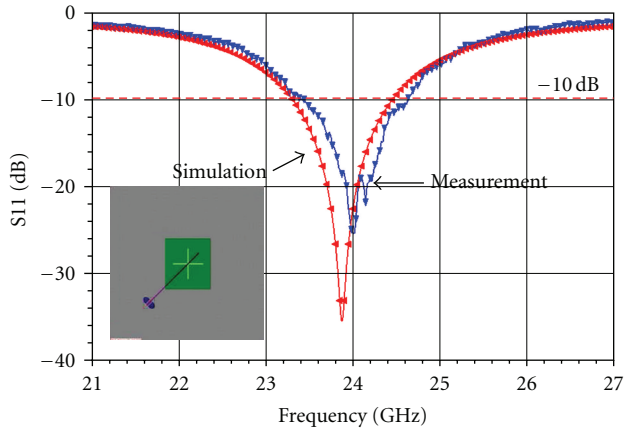

Figure 13: Measurement results of the input reflection coefficient of the dual mode patch antenna.

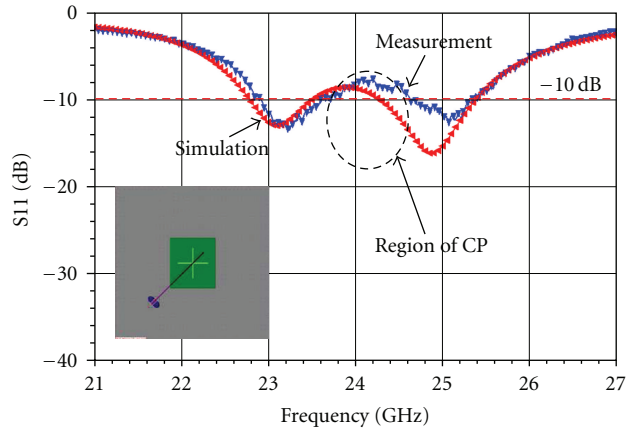

Figure 14: Measurement results of the input reflection coefficient of the circular polarized patch antenna.

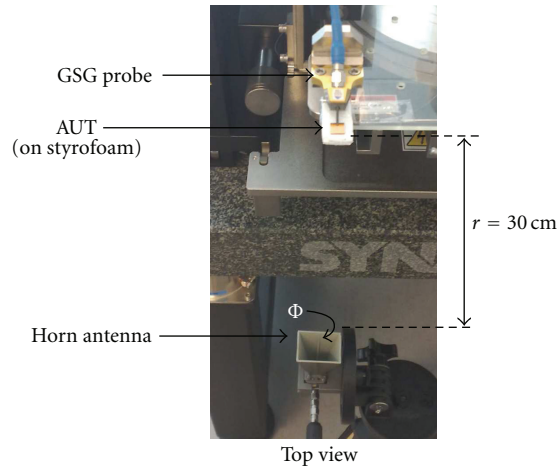

Figure 15: Setup for free-space transmission measurements of the antennas.

dimension of the aperture of the horn antenna is $d = 4$ cm. The far-field condition [21] is, hence, met at $r = 2d^2/\lambda = 25.6$ cm.

The transmission characteristics of the AUTs are extracted using the measured transmission factor S_{21} (obtained from the vector analyzer measurements) and including the loss by impedance mismatch a_{match} of the AUT, the free space loss a_{fs}, the gain of the horn antenna G_{horn} (for which calibrated data is available), and the additional measurement system attenuation caused by the cables and connectors a_{sys}.

$$Gain[dBi] = 20\log(|S_{21}|)[dB] + a_{match}[dB] + a_{fs}[dB] - G_{horn}[dBi] + a_{sys}[dB]. \quad (1)$$

The input match a_{match} must be considered because the AUTs are only matched well around their resonance frequencies. Therefore, a_{match} is included in the transmission equation with the following expression resembling the power fed to the antenna.

$$a_{match}[dB] = 10\log\left(1 - |S_{11}|^2\right)dB. \quad (2)$$

Note that the previously characterized reflection coefficients S_{11} of the AUTs are used. The frequency f and distance r dependent free space transmission loss a_{fs} given by Friis' transmission equation is calculated as follows [21]:

$$a_{\text{fs}}[\text{dB}] = -20\log\left(\frac{1}{4\pi r}\frac{c_0}{f}\right)\text{dB}. \quad (3)$$

The attenuation of the cables and connectors a_{sys} was measured by bypassing the antennas with a thru measurement. Together with the known gain of the horn antenna G_{horn} the normalized transmission is calculated. The horn antenna itself is well matched with a reflection coefficient <-10 dB across the measured bandwidth.

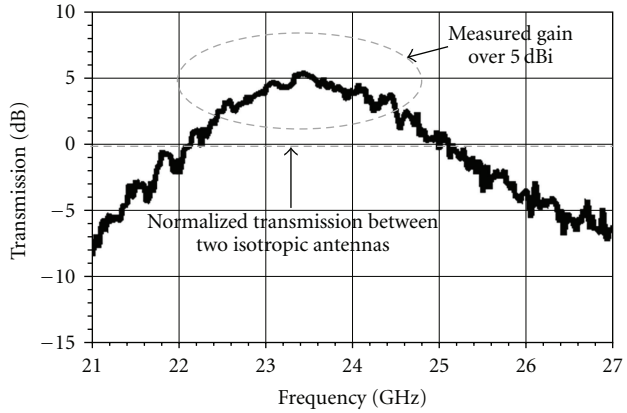

Figure 16: Measurement results of the transmission between the linear polarized patch antenna and the horn antenna.

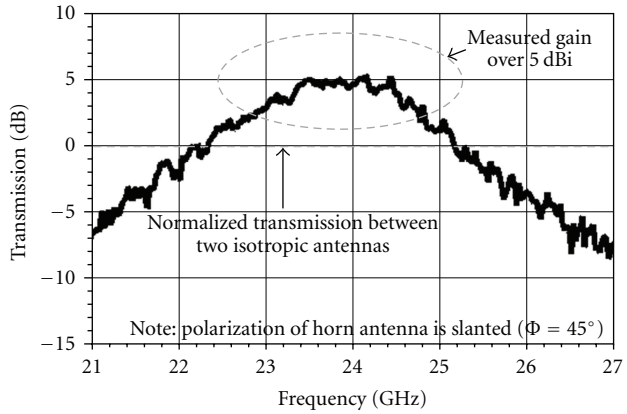

Figure 17: Measurement results of the transmission between the dual mode patch antenna and the horn antenna.

Figure 16 shows the measurement results of the LP patch antenna. In this measurement setup, the normalized transmission is 0 dB for two isotropic antennas separated by a distance of 30 cm. It was ensured that the polarizations of both antennas are matched. Around the resonance frequency of the LP patch antenna, the achieved gain is over 5 dBi compared to the normalized transmission. This matches well with the simulated gain of 5.5 dBi.

In Figure 17, the transmission of the DM patch antenna is shown. To ensure polarization matching between the horn antenna and the AUT, the horn antenna was rotated to $\Phi = 45^\circ$.

Finally, the CP patch antenna was also measured. The results are depicted in Figure 18. For this purpose, two measurements were conducted with two different horn antenna polarizations $\Phi = 0^\circ$ and 90°. It is observed that each mode is excited with similar amplitudes around their resonance frequencies. The resonance mode with the higher frequency is excited along the shorter patch side and vice versa. The two peaks are slightly shifted with respect to each other as was already shown on the reflection coefficient (see Figure 14). However, cross coupling between the two resonance modes

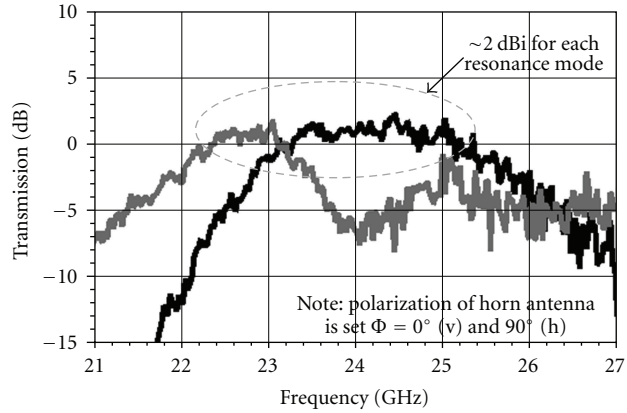

Figure 18: Measurement results of the transmission between the circular polarized patch antenna and the horn antenna.

must also be considered. As a result, not all the radiated power is transmitted (~2 dBi gain) with linear polarization at the resonance frequency of the respective mode and, hence, captured by the horn antenna. Therefore, the excitation of the two modes required for CP operation has been shown.

In conclusion, the functionality of the antennas has been shown experimentally.

5. Conclusions

Three compact 24 GHz patch antennas on glass substrates, suitable for integration in the top RF module of the wireless sensor node, were designed, characterized and compared. It was shown that efficient and highly integrated antennas can be manufactured using thin film WLP technologies. Gain values of more than 5 dBi as predicted by simulations were experimentally measured showing the feasibility of using this technology for antenna integration. In comparison to the LP patch antenna, the DM patch antenna shows higher impedance bandwidth while the CP patch antenna potentially allows more orientation flexibility for wireless sensor nodes.

Acknowledgments

The authors would like to thank the staff of the Fraunhofer IZM departments "High Density Interconnect and Wafer Level Packaging" and "System Integration & Interconnection Technologies" for their support in preparing the test wafers. Special thanks are extended to the project partners from the Technical University of Berlin, Ferdinand Braun Institute in Berlin, Friedrich Alexander University of Erlangen-Nürnberg and Technical University of Clausthal for the fruitful discussions and close collaboration. This work was conducted as part of the scientific project LOWILO (16SV365V) and is funded by the German Federal Ministry of Education and Research under the coordination of the VDI/VDE Innovation + Technik GmbH.

References

[1] M. Niedermayer, S. Guttowski, R. Thomasius, D. Polityko, K. Schrank, and H. Reichl, "Miniaturization platform for wireless sensor nodes based on 3D-packaging technologies," in *Proceedings of the 5th International Conference on Information Processing in Sensor Networks (IPSN '06)*, pp. 391–398, April 2006.

[2] R. Ebelt, H. Millner, and M. Vossiek, "Wireless network-to-network localization for measuring the spatial position and orientation of vehicles," in *Proceedings of the IEEE International Conference on Wireless Information Technology and Systems (ICWITS '10)*, Honolulu, Hawaii, USA, August 2010.

[3] F. Ohnimus, A. Podlasly, J. Bauer et al., "Electrical design and characterization of elevated antennas at PCB-level," in *Proceedings of the 59th Electronic Components and Technology Conference (ECTC '09)*, pp. 1618–1623, May 2009.

[4] P. R. Grajek, B. Schoenlinner, and G. M. Rebeiz, "A 24-GHz high-gain Yagi-Uda antenna array," *IEEE Transactions on Antennas and Propagation*, vol. 52, no. 5, pp. 1257–1261, 2004.

[5] T. Seki, N. Honma, K. Nishikawa, and K. Tsunekawa, "A 60-GHz multilayer parasitic microstrip array antenna on LTCC substrate for system-on-package," *IEEE Microwave and Wireless Components Letters*, vol. 15, no. 5, pp. 339–341, 2005.

[6] H. Reichl and M. J. Wolf, "System integration technologies for ultra small systems," in *Proceedings of the 11th IEEE International Symposium and Exhibition on Advanced Packaging Materials Processes, Properties and Interfaces*, p. 11, Atlanta, Ga, USA, 2006.

[7] P. K. Talukder, M. Neuner, C. Meliani, F. J. Schmückle, and W. Heinrich, "A 24 GHz active antenna in flip-chip technology with integrated frontend," in *Proceedings of the IEEE MTT-S International Microwave Symposium Digest*, pp. 1776–1779, June 2006.

[8] M. M. Hella, S. Devarajan, J. Q. Lu, K. Rose, and R. J. Gutmann, "Die-on-wafer and wafer-level 3D integration for millimeter-wave smart antenna transceivers," in *Proceedings of the IEEE Annual Conference on Wireless and Microwave Technology (WAMICON '05)*, pp. 125–128, April 2005.

[9] R. Carrillo-Ramirez and R. W. Jackson, "A highly integrated millimeter-wave active antenna array using BCB and silicon substrate," *IEEE Transactions on Microwave Theory and Techniques*, vol. 52, no. 6, pp. 1648–1653, 2004.

[10] J. G. Yook and L. P. B. Katehi, "Micromachined microstrip patch antenna with controlled mutual coupling and surface waves," *IEEE Transactions on Antennas and Propagation*, vol. 49, no. 9, pp. 1282–1289, 2001.

[11] P. M. Mendes, S. Sinaga, A. Polyakov, M. Bartek, J. N. Burghartz, and J. H. Correia, "Wafer-level integration of on-chip antennas and RF passives using high-resistivity polysilicon substrate technology," in *Proceedings of the 54th Electronic Components and Technology Conference*, pp. 1879–1884, June 2004.

[12] A. Latif, A. Oulad-Said, and A. A. Ouahman, "Passage from an inset-fed rectangular patch antenna to an end-fed and probe-fed rectangular patch antenna, modelling and analyses," in *Proceedings of the IEEE International Conference on Industrial Technology (ICIT '04)*, pp. 932–937, December 2004.

[13] B. M. Alarjani and J. S. Dahele, "Feed reactance of rectangular microstrip patch antenna with probe feed," *Electronics Letters*, vol. 36, no. 5, pp. 388–390, 2000.

[14] Y. Murakami, S. Sekine, and H. Shoki, "Analysis of cross-slot-coupled circular microstrip antenna," *Electronics Letters*, vol. 38, no. 25, pp. 1619–1621, 2002.

[15] B. Ai-Jibouri, T. Viasits, E. Korolkiewicz, S. Scott, and A. Sambell, "Transmission-line modelling of the cross-aperture-coupled circular polarised microstrip antenna," *IEE Proceedings: Microwaves, Antennas and Propagation*, vol. 147, no. 2, pp. 82–86, 2000.

[16] W. Yi, W. Lei, and S. Yunqing, "Design of L-circularly polarized microstrip antenna array at Ka band," in *Proceedings of the International Conference Microwave and Millimeter Wave Technology (ICMMT '10)*, Chengdu, China, May 2010.

[17] W. S. T. Rowe and R. B. Waterhouse, "Investigation of proximity coupled patch antennas suitable for MMIC integration," in *Proceedings of the International Symposium on Antennas and Propagation*, pp. 1591–1594, June 2004.

[18] S. Vajha and P. Shastry, "A novel proximity coupled patch antenna for active circuit integration," in *Proceedings of the IEEE Antennas and Propagation Society International Symposium-Adaptive Arrays in Communications-*, pp. 772–775, July 2001.

[19] D. G. Kim, C. B. Smith, C.-H. Ahn, and K. Chang, "A dual-polarization aperture coupled stacked microstrip patch antenna for wideband application," in *Proceedings of the IEEE International Symposium on Antennas and Propagation and CNC-USNC/URSI Radio Science Meeting—Leading the Wave (AP-S/URSI '10)*, Toronto, Canada, July 2010.

[20] B. Al-Jibouri, H. Evans, E. Korolkiewicz, E. G. Lim, A. Sambell, and T. Viasits, "Cavity model of circularly polarised cross-aperture-coupled microstrip antenna," *IEE Proceedings: Microwaves, Antennas and Propagation*, vol. 148, no. 3, pp. 147–152, 2001.

[21] C. A. Balanis, *Antenna Theory—Analysis and Design*, 2nd edition, 1997.